Particulate plutonium released from the Fukushima Daiichi meltdowns

Kurihara, Eitaro

2020-11-15

Kurihara , E , Takehara , M , Suetake , M , Ikehara , R , Komiya , T , Morooka , K , Takami , R , Yamasaki , S , Ohnuki , T , Horie , K , Takehara , M , Law , G T W , Bower , W , Mosselmans , J F W , Warnicke , P , Grambow , B , Ewing , R C & Utsunomiya , S 2020 , ' Particulate plutonium released from the Fukushima Daiichi meltdowns ' , The Science of the Total Environment , vol. 743 , 140539 . https://doi.org/10.1016/j.scitotenv.2020.140539

http://hdl.handle.net/10138/345949
https://doi.org/10.1016/j.scitotenv.2020.140539

unspecified
acceptedVersion

Submitted to *Science of the Total Environment*

Revision 1 submitted on

June 20th, 2020

Particulate plutonium released from the Fukushima Daiichi meltdowns

Eitaro Kurihara,[1] Masato Takehara,[1] Mizuki Suetake,[1] Ryohei Ikehara,[1] Tatsuki Komiya,[1] Kazuya Morooka,[1] Ryu Takami,[1] Shinya Yamasaki,[2] Toshihiko Ohnuki,[3] Kenji Horie,[4,5] Mami Takehara,[4] Gareth T. W. Law,[6] William Bower,[6] J. Frederick. W. Mosselmans,[7] Peter Warnicke,[8] Bernd Grambow,[9] Rodney C. Ewing,[10] and Satoshi Utsunomiya,[1,*]

[1]Department of Chemistry, Kyushu University, 744 Motooka, Nishi-ku, Fukuoka 819-0395, Japan

[2]Faculty of Pure and Applied Sciences and Center for Research in Isotopes and Environmental Dynamics, University of Tsukuba, 1-1-1 Tennodai, Tsukuba, Ibaraki 305-8577 Japan

[3]Laboratory for Advanced Nuclear Energy, Institute of Innovative Research, Tokyo Institute of Technology, 2-12-1 Ookayama, Meguro-ku, Tokyo 152-8550, Japan

[4]National Institute of Polar Research, 10-3, Midori-cho, Tachikawa-shi, Tokyo, 190-8518, Japan

[5]Department of Polar Science, The Graduate University for Advanced Studies (SOKENDAI),

Shonan Village, Hayama, Kanagawa, 240-0193, Japan

[6]Radiochemistry Unit, Department of Chemistry, The University of Helsinki, Helsinki Finland, 00014

[7]Diamond Light Source, Harwell Science and Innovation Campus, Didcot, Oxfordshire, OX11 0DE

[8]Swiss Light Source, Paul Scherrer Institute, 5232 Villigen, Switzerland

[9]SUBATECH, IMT Atlantique, CNRS-IN2P3, the University of Nantes, Nantes 44307, France

[10]Department of Geological Sciences and Center for International Security and Cooperation, Stanford University, Stanford, CA 94305-2115 USA

Corresponding author:

Satoshi Utsunomiya

Department of Chemistry, Kyushu University, 744 Motooka, Nishi-ku, Fukuoka 819-0395, Japan

Tel: +81-92-802-4168

E-mail: utsunomiya.satoshi.998@m.kyushu-u.ac.jp

Abstract

Traces of Pu have been detected in material released from the Fukushima Daiichi Nuclear Power Plant (FDNPP) in March of 2011; however, to date the physical and chemical form of the Pu have remained unknown. Here we report the discovery of particulate Pu associated with cesium-rich microparticles (CsMPs) that formed in and were released from the reactors during the FDNPP meltdowns. The Cs-pollucite-based CsMP contained discrete U(IV)O_2 nanoparticles, < ~10 nm, one of which is enriched in Pu adjacent to fragments of Zr-cladding. The isotope ratios, $^{235}U/^{238}U$, $^{240}Pu/^{239}Pu$, and $^{242}Pu/^{239}Pu$, of the CsMPs were determined to be ~0.0193, ~0.347, and ~0.065, respectively, which are consistent with the calculated isotopic ratios of irradiated-fuel fragments. Thus, considering the regional distribution of CsMPs, the long-distance dispersion of Pu from FNDPP is attributed to the transport by CsMPs that have incorporated nanoscale fuel fragments prior to their dispersion up to 230 km away from the Fukushima Daiichi reactor site.

Keywords

Uranium, Plutonium, Fuel fragment, Fukushima Daiichi, Cs-rich microparticle

50 1. Introduction

51 The nuclear disaster that occurred at the Fukushima Daiichi Nuclear Power Plant (FDNPP)
52 in March 2011 released $\sim 10^{19}$ Bq of radioactivity into the environment; this included fission
53 products (Xe, I, and Cs) (Buesseler et al., 2017; Steinhauser et al., 2014) and trace quantities of
54 actinides, such as U and Pu (Sakaguchi et al., 2014; Yamamoto et al., 2014; Zheng et al., 2013,
55 2012). In the reactor units #1 – 3, a large fraction of nuclear fuel, which is mainly composed of UO_2,
56 melted and caused the failure of each unit's reactor pressure vessel (RPV) (Nagase et al., 2016). The
57 melting fuel mixed with various structural materials, such as concrete and steel, and cooled to
58 remain as "debris" inside the reactors. The amount of U and Pu released from the FDNPP have been
59 estimated to be ~ 6.1×10^{-5} and 2.0×10^{-5} % of the core inventory, respectively (Sakaguchi et al.,
60 2014; Zheng et al., 2013). The Pu radioactivity in surface soils in the vicinity of the FDNPP was
61 determined to range from 0.003 to 3.924 Bq/kg (Yamamoto et al., 2014). The comparatively small
62 amount of released Pu was previously ascribed to the low volatility of U and Pu in nuclear fuel
63 (Grambow and Poinssot, 2012). Despite the limited amount of Pu in the environment surrounding
64 the FDNPP, the occurrence of Pu isotopes (half-lives of ^{238}Pu, ^{239}Pu, ^{240}Pu, and ^{241}Pu are 87.74 years,
65 2.411×10^4 years, 6563 years, and 14.35 years, respectively) have been a concern because of the
66 high effective dose conversion coefficient for these isotopes in the event of internal exposure ($1.5 \times$
67 10^{-5} Sv/Bq for ^{238}Pu, ^{239}Pu, and ^{240}Pu, 1.6×10^{-7} Sv/Bq for ^{241}Pu, and 1.4×10^{-5} Sv/Bq for ^{242}Pu)

68 (ICRP, 2012). Also, 32 of the 548 fuel assemblies in reactor unit 3 were a metal oxide fuel (MOX
69 fuel; U oxide mixed with ~3.9 wt % of Pu, $(U,Pu)O_2$).

70 Before the FDNPP meltdowns, the average isotope ratios of $^{235}U/^{238}U$, $^{240}Pu/^{239}Pu$, and
71 $^{242}Pu/^{239}Pu$ in the irradiated fuels of units 1 – 3 were calculated to be 0.0172 – 0.0193, 0.319 – 0.355,
72 and 0.0612 – 0.0654, respectively (Nishihara et al., 2012). Note that these values are only
73 representative isotope compositions averaged across the entire fuel inventory before meltdowns. A
74 significant heterogeneity likely occurred in the isotopic and chemical composition of the fuel debris
75 during, and possibly after the meltdowns.

76 Although intrinsic U and Pu oxide microparticles have been previously characterized in
77 various contaminated environments utilizing micro-focused X-ray analysis (e.g. Batuk et al., 2015;
78 Eriksson et al., 2005; IAEA, 2011; Ikeda-Ohno et al., 2016; Salbu et al., 2001), reports on the form
79 of U and Pu released from the FDNPP has been limited by the extremely low bulk Pu concentration
80 in regional soils, which is at the level of global, radioactive fall out from the testing of nuclear
81 weapons (Igarashi et al., 2019). However, the recent discovery of U oxides and fuel debris
82 microparticles associated with FDNPP derived Cs-rich microparticles (CsMPs) in the vicinity of the
83 site (Ochiai et al., 2018) raises the possibility that Pu might have been released together with U in
84 particulate form to the surrounding environment. The CsMPs are generally composed of Si, Fe, Zn,
85 and Cs; they are sparingly soluble and have high radioactivity per unit mass (~10^{11} Bq/g), and their

size ranges from submicron to tens of microns (Furuki et al., 2017; Ikehara et al., 2018; Imoto et al., 2017; Suetake et al., 2019; Utsunomiya et al., 2019) . The $^{134}Cs/^{137}Cs$ radioactivity ratio can be used to assign the source reactor because of the homogenized isotopic composition of the volatilized Cs (> ~670 ℃) within the damaged reactors, where temperatures approached ~2200 K. The $^{134}Cs/^{137}Cs$ radioactivity ratio of CsMPs is typically slightly over ~1 (Furuki et al., 2017), which agrees well with the ratios for units 2 (~1.08) and 3 (~1.05). The CsMPs formed inside the reactor were released, and dispersed over an area >10,000 km^2 in the Fukushima prefecture and Kanto region of eastern Japan (Adachi et al., 2013; Furuki et al., 2017; Ikehara et al., 2020, 2018; Utsunomiya et al., 2019; Yamasaki et al., 2016).

Another type of radioactive particle released from unit 1 of the FDNPP has been identified (Igarashi et al., 2019); however, this has not been defined as a CsMP because of its comparatively low Cs content (which is undetectable with energy dispersive X-ray analysis(EDX)). As a consequence, this type of particles was not investigated in the present study. Compared with CsMPs, the other type of particle is different in its physico-chemical properties; namely, they have a much lower Cs content and a different matrix composition, with a slightly lower $^{134}Cs/^{137}Cs$ radioactivity ratio of ~0.9. They are also larger (~several hundred μm) and are found in a limited area of distribution in the north-northwest zone close to the FDNPP. This distribution is linked to the direction of blast materials from the hydrogen explosion of unit 1. The presence and isotopic

104 signatures of Pu in this other type of radioactive particle have been recently investigated by
105 dissolution techniques (Igarashi et al., 2019). Based on a whole digestion and solution analysis, the
106 Pu isotopes were determined to be $^{240}Pu/^{239}Pu$ of 0.330 – 0.415 and $^{241}Pu/^{239}Pu$ of 0.162 – 0.178 with
107 large uncertainties; 9 – 23% (Igarashi et al., 2019), and thus it was difficult to be used as an explicit
108 isotopic signature for Pu.
109 Compared with the large radioactive particle derived from unit 1 distributed only within a
110 limited area near FDNPP, CsMPs of a smaller size were distributed across a wide area in the Kanto
111 region (up to 230 km away from FDNPP). The relation between CsMPs and long-range Pu transport
112 has been inferred in a previous study (Yamamoto et al., 2014), but the previous studies failed to
113 detect Pu in the CsMPs (Igarashi et al., 2019; Yamamoto et al., 2014). The purpose of the present
114 study is to elucidate the dispersion and release mechanisms of FDNPP-derived Pu into the
115 environment and to better understand the properties of the debris, in particular any occurrence of Pu.
116 This is based on a combination of advanced analyses of Pu and U isotopic signatures, speciation and
117 elemental distribution measurements, and characterization of the internal texture and structural
118 characteristics of individual CsMPs that have been released from the FDNPP units 2 or 3.
119
120 2. Samples and Methods
121 2.1. Samples

Soil samples were collected at an aqua culture center (AQC) and a paddy field in Ottozawa (OTZ), Okuma town, within ~ 4 km of the FDNPP (Fig. 1). Surface soils of the dimension of 20 cm × 20 cm × 2–5 cm depth were sampled from areas without vegetation. All of the collected soils were air dried and sieved through 2 mm Tetron mesh to remove pebbles and plants. Soil particles <2 mm were used for the present experiments. Isolation of three CsMPs was completed for three soil samples collected from the two locations, which were labelled as AQC1, AQC2, and OTZ.

2.2. Isolation of CsMPs

The procedure for separating CsMPs from soil samples followed the method developed in our previous study (Furuki et al., 2017). First, the soil samples were sieved through a 114-μm mesh. The samples were dispersed on an Al board and covered with a plastic sheet; an imaging plate (IP, Fuji film, BAS-SR 2025) was then placed on the samples for 5−25 minutes. The autoradiograph image was recorded with a pixel size of 100 μm using an IP reader (GE, Typhoon FLA 5100). After identifying the positions of intense radioactive spots, droplets of pure water were added to the positions and then taken up using a pipette to make a suspension with a small amount of soil particles. The procedure was repeated until the suspension did not contain a significant amount of soil particles. CsMPs are sparingly soluble because of the Si glass matrix (Suetake et al., 2019), as such, this procedure would not have affected the chemical properties of the CsMPs. Subsequently,

140 the position containing a highly radioactive spot was sampled using double-sided carbon tape. The
141 piece of carbon tape with the radioactive particle was cut into smaller pieces using a blade. The
142 small pieces were scanned again by autoradiography before a scanning electron microscopy (SEM)
143 observation. The pieces were placed on an Al plate and coated with carbon using a carbon coater
144 (SANYU, SC-701C) prior to SEM analysis. The CsMP was found using an SEM (Shimadzu, SS550
145 and Hitachi, SU6600) equipped with energy dispersive X-ray spectrometry (EDX, EDAX Genesis).
146 The acceleration voltage was 5−25 kV for imaging details of the surface morphology and 15−25 kV
147 for elemental analysis, including area analysis and elemental mapping.
148
149 2.3. Gamma spectrometry
150 ^{134}Cs and ^{137}Cs radioactivities of the three CsMPs were determined using gamma
151 spectrometry. The radioactivity of an additional micro-particle with a size of ~400 μm obtained from
152 the surface soil in Fukushima was precisely determined at the radioisotope center in Tsukuba
153 University, Japan, and utilized as a standard point specimen for ^{134}Cs and ^{137}Cs, which was used in a
154 previous study (Furuki et al., 2017). The radioactivity of the point source standard was 23.9 Bq for
155 ^{134}Cs and 94.6 Bq for ^{137}Cs as of September 29, 2015. The measurement of radioactivity was
156 performed on CsMPs and the point source standard using a gamma spectrometer equipped with a
157 low background type germanium detector GMX30200 (EG&G ORTEC Ltd.) in Tsukuba University,

158 Japan and Ge semiconductor detector GMX40 (SEIKO E&G) at the Center for Radioisotopes in
159 Kyushu University, Japan. The acquisition times were 4800 seconds for AQC using GMX30200 and
160 65878 s for OTZ using GMX40.
161
162 2.4. Secondary ion mass spectrometry
163 Isotopic ratio analysis was performed for the three CsMPs using secondary ion mass
164 spectrometry (SIMS, SHRIMP-II, Australian Scientific Instruments) at the National Institute of
165 Polar Research, Tokyo. The SIMS specimens were put on Al plates or a Cu grid and fixed on a glass
166 slide with Cu tape. They were coated with Au at a 13.5 nm thickness prior to the analysis. An O_2^-
167 primary ion beam of 0.2–0.4 nA was used to sputter the specimen surface with a beam diameter of
168 5.0–7.0 μm. The typical mass resolution is about 4,500 (M/ΔM at 1 % of peak height). Masses of
169 237.0 (or 253.0) and 242.1 (or 258.1) that is 0.1 amu heavier than ^{242}Pu, were measured as
170 background counts. The background ion counts were <0.04 cps in the CsMPs, which corresponds to
171 ~50 ppb. This value is considered to be the detection limit in the present study. The National
172 Institute of Standards and Technology (NIST) SRM610 was used as a standard specimen for mass
173 calibration, in which 461.5 mg/kg of depleted U was doped in a silicate glass matrix. Because
174 quantitative analysis using SIMS requires suitable standards, which have chemical compositions
175 similar to those of the target minerals, the absolute concentration was not obtained, but only the

176 isotopic ratio was determined in the present study. Ten scans were completed for each analytical spot
177 on the CsMPs, meaning that the sequence of ten analyses represents a depth profile of the variation
178 in the isotopic ratios; thus, SIMS analyses provide the isotopic signatures inside the CsMPs. The
179 effects of hydride on the U ion counts is considered to be negligibly small in the present study,
180 because isotope ratios of U ions are almost same as those of UO ions during measurement of
181 SRM610 despite the fact that probability of hydride formation from a UO ion is less than that of U
182 ion (Morrall et al., 2007). In addition, a mass ^{237}(^{236}UH) was also measured in the present analysis
183 and the count was at the background level in all measurements.
184
185 2.5. Synchrotron Analysis
186 After performing SIMS analysis, X-ray fluorescence (XRF) mapping and discrete-area
187 X-ray absorption near-edge spectroscopy (XANES) was completed at beamlines I18, at
188 Diamond Light Source, UK, and X05LA at the Swiss Light Source. In both instances, AQC1
189 was mounted on carbon tape and double contained in Kapton windowed radioactive sample
190 holders for analysis.
191 At beamline I18 (double-crystal monochromator), the synchrotron micro-beam was
192 focused to a horizontal width of ~2 μm. XRF mapping was performed with an incident beam
193 energy of 18.1 keV. Uranium and Pu L_{III}-edge XANES data were collected in fluorescence mode

194 at ambient temperature with minimum step sizes of 0.1 eV and 0.5 eV over the absorption edges
195 of U and Pu, respectively. Fluorescence data were collected using the beamline's 4 element
196 Vortex Silicon Drift Diode (SDD). Uranium (IV/VI) reference standards were the research
197 teams own, with data collected on beamline B18 at the Diamond Light Source (calibrated using
198 in-line Y foil). The U(IV) standard is a crystalline uraninite (UO_2) powder and the U(VI)
199 standard is a crystalline metaschoepite ($UO_3 \bullet nH_2O$) powder. Plutonium standards were not run.

200 At beamline X05LA (double-crystal monochromator), the synchrotron micro beam
201 was focused to a horizontal width of ~ 1 μm. On-the-fly XRF maps, windowed for Fe, Zn, Zr,
202 Mn, Sr, and U were collected at incident beam energies of 18.0 and 18.1 keV. Pu L_{III}-edge
203 XANES data were collected in fluorescence mode at ambient temperature with a step size of 0.5
204 eV over the absorption edge. Fluorescence data was collected using the beamlines'
205 single-element Ketek SDD. At both beamlines, Y and Zr foils were used to calibrate the U and
206 Pu absorption edges, respectively. XRF mapping data were processed using PyMCA (Solé et al.,
207 2007). Although μXRF analysis was not used for quantitative elemental analysis in the present
208 study, the synchrotron-based XRF facilities used at both beam-lines can typically analyze U and
209 Pu down to concentrations of several 10s of ppm. Maps were normalized for comparability by
210 subtracting the base noise level from the maps and dividing the maps by the maximum pixel
211 intensity. XANES data were aligned and normalized using Athena (Demeter Suite) (Ravel and

212 Newville, 2005).

213

214 2.6. Transmission electron microscopy (TEM) analysis and the specimen preparation

215 High-resolution TEM (HRTEM) with energy dispersive X-ray analysis (EDX) and
216 high-angle annular dark-field scanning transmission electron microscopy (HAADF-STEM)
217 were performed using a JEOL JEM-ARM200F with an acceleration voltage of 200 kV at the
218 Ultramicroscopy Research Center (URC) of Kyushu University. The spatial resolution is ~0.11
219 nm. The JEOL Analysis Station software was used to control the STEM-EDX mapping. To
220 minimize the effect of sample drift, a drift-correction mode was used during acquisition of the
221 elemental map. The detection limit of EDX analysis is typically ~0.1 wt%. The STEM probe
222 size was ~0.13 nm, generating ~140 pA of current when 40 μm of the condenser lens aperture
223 was inserted. The collection angle of the HAADF detector was ~97–256 mrad.

224 A focused ion beam (FIB) system (FEI, Quanta 3D FEG 200i Dual Beam) was utilized
225 to prepare thin foils of AQC1 after SIMS and synchrotron X-ray analysis. The ion source was
226 Ga, while W deposition was used to minimize damage by the ion bombardment covering a
227 rectangle area of ~3×8 μm size (Fig. S1a). The current and acceleration voltage of the ion beam
228 were adjusted to be 100 pA to 30 nA and 5–30 kV depending on the progress of thinning and
229 sample properties such as hardness and size. The thinned piece of size of ~2 × 6 × 5 μm was

attached to the semilunar-shaped Cu grid for FIB and further thinned to < 200 nm thickness by an ion beam at 5 or 8 kV.

The above analysis was performed in the order of SIMS > μ-focus X-ray analysis > TEM, so that the CsMPs containing U and Pu can be efficiently analyzed. Due to the limited size of the samples compared with the SIMS ion probe, AQC2 and OTZ were entirely consumed during SIMS analysis and the further analyses could not be performed. The μ-focus X-ray analysis and TEM were competed only for sample OTZ1.

3. Results and Discussion

3.1. Occurrence of U and Pu in the CsMPs revealed by the advanced nano-scale analyses

In the present study, three CsMPs, labelled as AQC1, AQC2, and OTZ, were isolated from the surface soils sampled within 3.9 km of the FDNPP (Fig. 1 and Table 1). Secondary electron images from scanning electron microscopy (SEM), energy dispersive X-ray analysis (EDX) elemental maps, and the resulting spectra revealed a morphology and major element composition (Si, Fe, Zn, Cs, and O) typical of CsMPs reported in the literature (Furuki et al., 2017; Ikehara et al., 2018; Ochiai et al., 2018) (Fig. 2a – c). AQC1 occurs as an aggregate of smaller CsMP particles, while AQC2 and OTZ are individual microparticles. In all EDX spectra, Al concentrations may have

248 been enhanced due to background soil materials. The amount of the other major and minor elements
249 such as Fe, Zn, and Sn are similar to that of CsMPs previously reported (Furuki et al., 2017; Imoto et
250 al., 2017; Utsunomiya et al., 2019), and they are derived from structural materials such as stainless
251 steel, Zr-Sn alloy claddings, and primary cooling water (that contained Zn) (Abe et al., 2014). In the
252 CsMPs, the total radioactivities of ^{134}Cs and ^{137}Cs per unit mass are in the order of 10^{11} Bq/g, and the
253 $^{134}Cs/^{137}Cs$ radioactivity ratios range from 1.05 to 1.17 after decay-correction to March 11th, 2011.
254 This demonstrates that the CsMPs originated from the volatilized Cs stemming from molten fuel
255 inside the damaged FDNPP reactor units 2 or 3 (Table 2). In general, the CsMPs were considered to
256 form through molten core-concrete interaction at the concrete pedestal of the primary containment
257 vessel, where the volatilized Cs, stemming from molten fuel, was condensed with vaporized silica
258 (Furuki et al., 2017).

259 Synchrotron micro-focus X-ray fluorescence (μXRF) mapping was successfully performed
260 on AQC. Mapping of the whole particle showed that the distribution of Fe was slightly different to
261 Zn (Fig. 3a). Further detailed mapping of the area outlined by the white dotted rectangle in the Fe
262 map of Fig. 3a also revealed heterogeneously localized distributions of U, Zr, Sr (Sr masked any Pu
263 signal) and Mn within AQC, implying that the melted fuel fragment reacted heterogeneously with
264 Zr-containing fuel cladding at the micron-scale. Indeed, prior work has characterized nanoparticles
265 of (U, Zr) oxide solid solution containing a wide range of U/Zr ratios (Ochiai et al., 2018).

Iterative-target factor analysis (ITFA) (Rossberg et al., 2003) of the U L_3-edge μXANES (Fig. 3b), collected from the point indicated by red arrow (Fig. 3a), and comparison with U(IV) and U(VI) standards, suggests that the U predominantly occurs as U(IV) oxide (*i.e*. there was no meaningful spectral contribution from U(VI)) (Fig. 3b).

Plutonium XRF mapping was attempted; however, it was hampered due to interference from Sr. Within the U distribution map, the three spots with highest U intensity (indicated by the arrows in Fig. 3a) were further analyzed in an attempt to obtain X-ray absorption spectra at the Pu L_3 edge. In the three areas of highest U, two spots (indicated by the white arrows) did not show a Pu absorption edge; in contrast, the area indicated by the red arrow had enough Pu to permit collection of an absorption edge, albeit of low quality (Fig. 3c). Given the noise in the data and to ensure reproducibility, the Pu L_3 edge XANES spectrum was collected from the same point in the sample at both micro-focus beamlines used in this study (Fig. 3c). This highlights Pu occurrence within the CsMP and represents the first Pu XANES spectrum collected from Fukushima soils, where Pu is present at levels similar to global fallout. Whilst the low signal to noise ratio precludes confident evaluation of the Pu speciation in the CsMP inclusion, the shape of the spectrum at least indicates that the Pu occurs as a Pu oxide (*e.g*. Ankudinov et al., 1998; Conradson et al., 2004) , and not as Pu metal, which has a reduced XANES amplitude (*e.g*. Clark and Hobart, 2019; Ikeda-Ohno et al., 2016).

284 A thin foil for TEM observation was then made from the part of AQC1 indicated by a red
285 rectangle in Fig. S1a using a focused ion-beam system to investigate textural and structural
286 characteristics. A cross sectional view in HAADF-STEM images and EDX elemental maps of major
287 elements revealed that AQC consists of a variety of nano-phases including Cs-pollucite (Cs-Fe
288 silicate), ilmenite (Fe-Ti oxide), magnetite (Fe oxide), and chromite (Fe-Cr oxide), based on the
289 diffraction pattern and composition (Fig. 2b and Fig. S1b – e). Although a typical CsMP comprises a
290 SiO_2 glass matrix with Fe, Cs, and Zn, Cs-pollucite is a zeolite phase that can form within CsMPs
291 when the Cs concentration is extremely high (> 10 wt.% ;Imoto et al., 2017). Closely associated with
292 the Fe oxides, several U oxide nanoparticles were also found as indicated by yellow and red arrows
293 in Fig. 4a, which are labeled from U1 to U4 (Fig. 4b and Fig. S2). A high-resolution HAADF-STEM
294 image of U4 indicated by the red arrow revealed a periodic array of U atoms corresponding to the
295 (111) plane of uraninite (Fig. 4c), indicating that U dioxide nanoparticles were encapsulated during
296 the formation of the CsMP, as reported in our previous study (Ochiai et al., 2018) and as indicated
297 from the U L3-edge XANES (Fig. 3b). The scattered occurrence of uraninite nanoparticles within
298 AQC is consistent with the heterogeneous U distribution observed in the μXRF map (Fig. 3a), which
299 does not correlate with the distribution of other elements within CsMP.
300 Based on the results obtained from TEM, XRF elemental mapping, and XANES analyses,
301 U predominantly occurs as U(IV) oxide in the CsMP, with small Pu oxide-enriched areas also

302 present. As such, the particle appears to be a debris fragment with fuel composition that has been
303 minimally affected by the subsequent alteration owing to its encapsulation in the CsMP. With
304 increasing burn-up, actinides such as Np, Pu, and Am substitute for U in UO_2 matrix (Konings et al.,
305 2015); thus, the trace Pu is distributed within the UO_2 matrix. The maximum value of burn-up: 40
306 GWd/tHM for both units 2 and 3 (Nishihara et al., 2012), is high enough to have Pu concentrates at
307 fuel edge sites due to the higher burn-up (Bruno and Ewing, 2006; Burns et al., 2012; Ewing, 2015).
308 Hence, the slightly enhanced Pu concentration, likely at ppm level, detected by μ-focus XANES
309 within the UO_2 matrix is plausibly derived from a Pu concentrate at the rim of irradiated fuel, where
310 a U, Zr oxide eutectic formed as inferred from localized Zr occurrence (Fig. 3) and also
311 characterized in another CsMP utilizing TEM (Ochiai et al., 2018). Because the nuclear fuel
312 fragment was not subjected to significant alteration, the initial state of Pu(IV) that substitutes for U
313 in the irradiated UO_2 (Ewing, 2015; Konings et al., 2015) has remained in its initial state, which is
314 consistent with the XANES data that indicates Pu is present as an oxide.
315
316 3.2. Plutonium and U isotope ratios in the CsMPs
317 Secondary ion mass spectrometry (SIMS) was successfully applied to determine U and Pu
318 isotopes in these three CsMPs (Table 3). During SIMS analysis, the ionized isotopes were detected
319 either in non-oxide ion or oxide ion form. Oxide form means an element bound to oxygen such as

320 $^{235}U^{16}O$, of which the total mass of 251 is measured. The non-oxide form of ionized isotopes was
321 detected for two analytical spots in AQC1, one spot in AQC2, and one spot in OTZ, whilst oxide
322 ions were only detected for two spots in AQC1 and one spot in AQC2, due to the limited sample
323 volume for OTZ (the OTZ CsMP was consumed by the first set of analysis detecting the non-oxide
324 ion form and could not be used for the second set of analysis detecting the oxide ion form). As
325 revealed in Fig. 5 and Table 3, isotope ratios in non-oxide and oxide form revealed almost identical
326 values for $^{235}U/^{238}U$ and $^{239}Pu/^{238}U$, but the greater number of ions were counted for the oxide form.
327 The $^{235}U/^{238}U$ isotope ratios of the four analyzed spots are 0.01935 (± 0.00009), 0.01935 (± 0.00006),
328 0.01935 (± 0.00011), and 0.01925(± 0.00014), and the ^{238}U ion count ranges from 835 to 975
329 (cps/nA) (Fig. 5a, Table 3). The isotope ratio is nearly identical to that calculated for the irradiated
330 fuel of units 2 or 3 based on the burnup using ORIGEN2 code; ~0.019 (Nishihara et al., 2012). In
331 our previous study (Imoto et al., 2017), the $^{235}U/^{238}U$ isotope ratio of the analyzed CsMPs was
332 determined to be ~0.029 with low ^{238}U counts; 11 – 14 cps/nA. These ratios plotted between that of
333 non-irradiated fuel (0.039) and irradiated fuel (0.019), which was ascribed to volatilization of a
334 partially oxidized form of the less-irradiated fuel, as evidenced by the low ^{238}U counts. In contrast,
335 the total ^{238}U counts detected in the present study are nearly two orders of magnitude greater than
336 that derived from U volatilization, with the $^{235}U/^{238}U$ isotope ratio identical to that of the irradiated
337 fuel (Fig. 5a). This is a strong indication that the SIMS analysis spots included discrete fuel particles

within the CsMPs as revealed by the TEM results (Fig. 4, Fig. S2) rather than trace and diluted U sorbed to the CsMP matrix, subsequent to volatilization, as reported in a previous study (Imoto et al., 2017). Nanoparticulate uranium dioxides and (U, Zr)-oxide solid solutions were also identified to be associated with CsMPs (Ochiai et al., 2018). Despite that the burnup of the irradiated fuel at the time of nuclear disaster ranged from 3.3 to 40 GWd/tHM for unit 2 and from 4.5 to 40 GWd/tHM for unit 3 (Nishihara et al., 2012), the $^{235}U/^{238}U$ isotope ratios determined in the present study are identical to the isotope ratios averaging the entire fuel assemblies in each reactor. This indicates either the formation of large-scale melting of fuel rods so that the U isotopic ratio was homogenized, or the burnup of U oxide analyzed by SIMS in the present study is coincidentally close to the average value of the irradiated fuels in FDNPP at the time of meltdowns.

In general, a series of Pu isotopes are produced mainly through the following sequence of nuclear reactions in reactors (Choppin et al., 2002);

$$\underset{(2.411\times10^{4}\ \mathrm{y})}{^{239}\mathrm{Pu}}\ (n,\gamma)\ \underset{(6564\ \mathrm{y})}{^{240}\mathrm{Pu}}\ (n,\gamma)\ \underset{(14.35\ \mathrm{y})}{^{241}\mathrm{Pu}}\xrightarrow{\beta^-}\underset{(432.2\ \mathrm{y})}{^{241}\mathrm{Am}}\ (n,\gamma)\ \underset{(16.02\ \mathrm{h})}{^{242}\mathrm{Am}}\xrightarrow[\beta^-\ (82.7\ \%)]{\mathrm{EC}\ (17.3\ \%)}\underset{(3.75\times10^{5}\ \mathrm{y})}{^{242}\mathrm{Pu}},\ ^{242}\mathrm{Cm} \quad (1)$$

, in which the time in parentheses represents the half-life of the respective radionuclide. The analyzed Pu isotopes are listed in Table 3. Because the isotope ratio of $^{239}Pu/^{238}U$ was almost identical between non-oxide and oxide forms (Fig. 5b), the following discussion describes Pu-oxide ion ratios simply as a Pu isotope ratio. Plutonium isotope ratios of two spots in AQC1 are plotted in

355 Fig. 5c and exhibit clear difference from the values of global fallout (Kelley et al., 1999). The
356 isotope ratio of Pu, $^{240}Pu/^{239}Pu$, was determined to be 0.3492 (± 0.0040) for AQC1-spot1, 0.3441 (±
357 0.0033) for AQC1-spot2, and 0.3313 (± 0.0114) for AQC2, which are close to those of the average
358 Pu vector calculated using ORIGEN2 for the irradiated fuels at the time of disaster in the FDNPP
359 (Nishihara et al., 2012). This is consistent with the results analyzed for bulk soils and litter samples
360 in previous studies (Zheng et al., 2013, 2012). The other results calculated using ORIGEN ARP
361 (Kirchner et al., 2012; Schwantes et al., 2012) and CASMO5 (Yamamoto et al., 2018) revealed
362 slightly higher $^{240}Pu/^{239}Pu$ isotope ratios. The isotopic ratio of $^{242}Pu/^{239}Pu$ was determined to be
363 0.0668 (± 0.0033), 0.0651 (± 0.0011), and 0.0622 (± 0.0059), which are plotted within the range of
364 the calculated ratios by ORIGEN2 (Nishihara et al., 2012), ORIGEN ARP (Kirchner et al., 2012;
365 Schwantes et al., 2012), and CASMO5 (Yamamoto et al., 2018). For comparison, the Pu isotope
366 ratios were calculated using ORIGEN ARP for the MOX fuels irradiated for 171 days prior to the
367 meltdowns with input data of the fuel at the time of loading (Nishihara et al., 2012), because the Pu
368 concentration was as high as ~2.8 wt% (Nishihara et al., 2012) and occupied 32 of the 548 fuel
369 assemblies in the unit 3 (Nuclear Emergency Response Headquarters and Government of Japan,
370 2011) leading to the serious concerns of radiotoxicity. The relationship between Pu isotopes clearly
371 indicates that the Pu is not derived from MOX.
372 The ratio of the $^{239}Pu/^{238}U$ ion count was calculated to be 0.00488 (± 0.00020) and 0.00490

373 (± 0.00010) for two spots in AQC1, 0.01011 (± 0.00031) for AQC2, and 0.00534 (± 0.00037) for
374 OTZ (Fig. 5b, Table 3). Figure 5b also indicates that the ionization efficiency of the non-oxide is
375 essentially the same as that of the oxide forms for U and Pu in the CsMP matrix. The wide range in
376 the ratios for the three analytical points from 0.0048 to 0.01011 also indicates that the Pu content in
377 the U oxide matrix can vary within the volume of SIMS microanalysis (~4 – 5 μm) and between the
378 different CsMPs.
379
380 3.3. Release process of fuel fragments, environmental effects, and insights to debris
381 In early studies, the release of Pu from the FDNPP was considered to occur through
382 volatilization and the amount of Pu released was estimated relative to that of Cs. This was based on
383 the assumption that Pu isotopes and ^{137}Cs were released from the reactors following the same
384 general fate in the meltdown environment (Zheng et al., 2013). Schwantes et al. (2012) proposed that
385 the relative amount of released Pu was proportional to its volatility, which in turn is correlated with
386 its Gibbs free energy of formation at 1000 K (Schwantes et al., 2012). However, experimental
387 studies have revealed that the volatility of Pu is lower than that of U (Pontillon et al., 2010; Pontillon
388 and Ducros, 2010), and the amount of Pu released through volatilization has been considered to be
389 negligible in the FDNPP (Grambow and Poinssot, 2012). In addition, ambiguity remained for the
390 wide range of Pu radioactivity in bulk soil samples (Sakaguchi et al., 2014; Yamamoto et al., 2014).

391 This is partly ascribed to the difference in the form of the released Cs; soluble Cs and CsMPs, which
392 formed through different processes and timing (Furuki et al., 2017). The distribution of Pu is not
393 identical to that of Cs. Rather, the scattered occurrence of trace Pu in the surrounding environments
394 reported in the previous studies (Sakaguchi et al., 2014; Yamamoto et al., 2014) is attributed to the
395 Pu transport in the form of microparticles as inferred in the previous study (Kirchner et al., 2012;
396 Zheng et al., 2012). As shown in the micro XRF maps in Fig. 3, Zr occurrence is heterogeneous,
397 indicating that the UO_2 in the CsMP was not subject to the homogenization or volatilization and that
398 the fuel fragment itself was captured by the CsMP and released to the environment through the same
399 mechanisms reported previously (Ochiai et al., 2018). This is the direct evidence of Pu release along
400 with fuel fragments that has never been reported for the FDNPP.
401 In general, the particulate occurrence of Pu affects the mobility, bioavailability,
402 transportation, and dose conversion factors, depending on the physicochemical properties (Salbu and
403 Lind, 2016). As shown in previous studies, the scattered distribution of Pu derived from the FDNPP
404 was observed in the large area at >50 km of radial distance affected by radioactive Cs released from
405 units 2 and/or 3 (Sakaguchi et al., 2014; Yamamoto et al., 2014), while CsMPs were ubiquitously
406 distributed in the area (Ikehara et al., 2018). This suggests that even though fuel fragments were
407 found to be associated with CsMPs in the present study, not all CsMPs contained the fragments
408 when they were released and transported over large distances. In addition, it is highly probable that

409 other fuel fragments were also released directly without association with CsMPs during the
410 explosive events; however, the size must be small enough to allow them to be transported over long
411 distances. Although the discovery of a particulate form of Pu released from the FDNPP may raise the
412 potential risk of Pu uptake, even at large distances from the FDNPP, the Pu radioactivity in bulk
413 samples does not exceed the range of radioactivity from global fallout from the testing of nuclear
414 weapons (MEXT and GSI, 2012; Zheng et al., 2013). Such a low concentration of Pu may not have
415 significant health effects (Taylor, 1995); however, the actual interaction mechanism can be more
416 complicated depending on the occurrence of fuel fragments in CsMPs; either attaching onto the
417 surface or encapsulated by the CsMP.

418 The present study highlights that the fuel fragments containing Pu were released from the
419 reactors to the surrounding environment associated with micron-scale CsMPs. These fuel fragments
420 provide partial but direct information on the processes that the nuclear fuels experienced during the
421 meltdowns, as well as on the current status of debris. Notably, other fissionogenic radionuclides,
422 such as Sr are also associated with the fuel fragment, which is also consistent with the very
423 low-volatility of Sr (Pontillon and Ducros, 2010). These results also suggest that the concentrations
424 of Pu isotopes in the fuel composition of the debris can be reasonably estimated by using a code such
425 as ORIGEN. Currently, the radiation doses are still too high to access inside the reactors; ~11 and
426 ~80 Sv/h within primary containment vessels (PCVs) of units 1 and 2 in 2017, respectively (Tokyo

427 Electric Power Company Holdings, 2018, 2017). Direct characterization of fuel fragments that were
428 released to the environment (or collected from preliminary investigations inside the reactors using
429 robots) is of crucial importance for understanding the properties of the debris prior to its removal in
430 the course of decommissioning, which is expected to require several decades.
431
432
433

Author Contributions

S.U. conceived the idea and designed all experiments. E.K. and S.U. wrote the manuscript. M.S., T.K., K.M., and R.I. performed separation of CsMPs and SEM analysis. T.O. provided navigation during field research in Fukushima. S.Y. performed gamma spectroscopy. K.H. and M.T. performed SIMS analysis. G.T.W.L., W.R.B., J.F.W.M., and P.W. performed the SR-μXRF and μXAFS analysis. G.T.W.L, W.R.B., B.G., R.C.E., J.F.W.M participated in the discussion and interpretation of the results and helped to write the manuscript.

Acknowledgments

The authors are grateful to Dr. Watanabe for her assistance on SEM analyses at the Center of Advanced Instrumental Analysis, Kyushu University. This study is partially supported by JST Initiatives for Atomic Energy Basic and Generic Strategic Research and by a Grant-in-Aid for Scientific Research (KAKENHI) from the Japan Society for the Promotion of Science (16K12585, 16H04634, JP26257402). S.U. is also supported by The Mitsubishi Foundation/Research Grants in the Natural Sciences, Environmental Radioactivity Research Network Center (F-19-03), and by ESPEC Foundation for Global Environment Research and Technology (Charitable Trust) (ESPEC Prize for the Encouragement of Environmental Studies). G.T.W.L. and W.R.B acknowledge UK NERC funding (NE/ M014088/1). The Diamond Light Source (NT21211-1) and the Swiss Light

452 Source (20181008) are thanked for analysis time, and Connaugh Fallon (University of Manchester)
453 is thanked for assisting with the SR-μXRF and XANES analysis. R.C.E. was partially supported by
454 the U.S. Department of Energy, National Nuclear Security Administration, Office of Defense
455 Nuclear Nonproliferation Research and Development under Contract No. DE-AC02-76SF00515.
456 The findings and conclusions by the authors of this paper do not necessarily state or reflect those of
457 the JST.
458

459 **References**

460 Abe, Y., Iizawa, Y., Terada, Y., Adachi, K., Igarashi, Y., Nakai, I., 2014. Detection of uranium and

461 chemical state analysis of individual radioactive microparticles emitted from the Fukushima nuclear

462 accident using multiple synchrotron radiation X-ray analyses. Anal. Chem. 86, 8521–8525.

463 https://doi.org/10.1021/ac501998d

464 Adachi, K., Kajino, M., Zaizen, Y., Igarashi, Y., 2013. Emission of spherical cesium-bearing particles

465 from an early stage of the Fukushima nuclear accident. Sci. Rep. 3, 2554.

466 https://doi.org/10.1038/srep02554

467 Ankudinov, A.L., Conradson, S.D., Mustre de Leon, J., Rehr, J.J., 1998. Relativistic XANES calculations

468 of Pu hydrates. Phys. Rev. B 57, 7518–7525. https://doi.org/10.1103/PhysRevB.57.7518

469 Batuk, O.N., Conradson, S.D., Aleksandrova, O.N., Boukhalfa, H., Burakov, B.E., Clark, D.L.,

470 Czerwinski, K.R., Felmy, A.R., Lezama-Pacheco, J.S., Kalmykov, S.N., Moore, D.A., Myasoedov,

471 B.F., Reed, D.T., Reilly, D.D., Roback, R.C., Vlasova, I.E., Webb, S.M., Wilkerson, M.P., 2015.

472 Multiscale Speciation of U and Pu at Chernobyl, Hanford, Los Alamos, McGuire AFB, Mayak, and

473 Rocky Flats. Environ. Sci. Technol. 49, 6474–6484. https://doi.org/10.1021/es506145b

474 Bruno, J., Ewing, R.C., 2006. Spent nuclear fuel. Elements 2, 343–349.

475 https://doi.org/10.2113/gselements.2.6.343

476 Buesseler, K., Dai, M., Aoyama, M., Benitez-Nelson, C., Charmasson, S., Higley, K., Maderich, V.,

Masqué, P., Morris, P.J., Oughton, D., Smith, J.N., 2017. Fukushima Daiichi–derived radionuclides in the ocean: transport, fate, and impacts. Ann. Rev. Mar. Sci., Annual Review of Marine Science 9, 173–203. https://doi.org/10.1146/annurev-marine-010816-060733

Burns, P.C., Ewing, R.C., Navrotsky, A., 2012. Nuclear Fuel in a Reactor Accident. Science (80-.). 335, 1184–1188. https://doi.org/10.1126/science.1211285

Choppin, G.R., Liljenzin, J.-O., Rydberg, J., 2002. Radiochemistry and Nuclear Chemistry, 3rd Editio. ed. Butterworth-Heinemann, Woburn, MA.

Clark, D.L., Hobart, D.E., 2019. Discovery of the Transuranium Elements Inspired Rearrangement of the Periodic Table and the Approach for Finding New Elements, in: D. Michael P. Mingos (Ed.), The Periodic Table I. Springer, Cham, pp. 225–259. https://doi.org/10.1007/430_2019_46

Conradson, S.D., Abney, K.D., Begg, B.D., Brady, E.D., Clark, D.L., den Auwer, C., Ding, M., Dorhout, P.K., Espinosa-Faller, F.J., Gordon, P.L., Haire, R.G., Hess, N.J., Hess, R.F., Keogh, D.W., Lander, G.H., Lupinetti, A.J., Morales, L.A., Neu, M.P., Palmer, P.D., Paviet-Hartmann, P., Reilly, S.D., Runde, W.H., Tait, C.D., Veirs, D.K., Wastin, F., 2004. Higher Order Speciation Effects on Plutonium L 3 X-ray Absorption Near Edge Spectra. Inorg. Chem. 43, 116–131. https://doi.org/10.1021/ic0346477

Eriksson, M., Osán, J., Jernström, J., Wegrzynek, D., Simon, R., Chinea-Cano, E., Markowicz, A., Bamford, S., Tamborini, G., Török, S., Falkenberg, G., Alsecz, A., Dahlgaard, H., Wobrauschek, P.,

Streli, C., Zoeger, N., Betti, M., 2005. Source term identification of environmental radioactive Pu/U particles by their characterization with non-destructive spectrochemical analytical techniques. Spectrochim. Acta Part B At. Spectrosc. 60, 455–469. https://doi.org/10.1016/j.sab.2005.02.023

Ewing, R.C., 2015. Long-term storage of spent nuclear fuel. Nat. Mater. 14, 252–257. https://doi.org/10.1038/nmat4226

Furuki, G., Imoto, J., Ochiai, A., Yamasaki, S., Nanba, K., Ohnuki, T., Grambow, B., Ewing, R.C., Utsunomiya, S., 2017. Caesium-rich micro-particles: A window into the meltdown events at the Fukushima Daiichi Nuclear Power Plant. Sci. Rep. 7, 42731. https://doi.org/10.1038/srep42731

Grambow, B., Poinssot, C., 2012. Interactions between nuclear fuel and water at the Fukushima Daiichi reactors. Elements 8, 213–219. https://doi.org/10.2113/gselements.8.3.213

IAEA, 2011. Radioactive particles in the Environment: Sources, Particle Characterization and Analytical Techniques. IAEA in Austria, Vienna, Austria.

ICRP, 2012. Compendium of Dose Coefficients based on ICRP Publication 60. Ann. ICRP ICRP Publi.

Igarashi, J., Zheng, J., Zhang, Z., Ninomiya, K., Satou, Y., Fukuda, M., Ni, Y., Aono, T., Shinohara, A., 2019. First determination of Pu isotopes (239Pu, 240Pu and 241Pu) in radioactive particles derived from Fukushima Daiichi Nuclear Power Plant accident. Sci. Rep. 9, 11807. https://doi.org/10.1038/s41598-019-48210-4

Ikeda-Ohno, A., Shahin, L.M., Howard, D.L., Collins, R.N., Payne, T.E., Johansen, M.P., 2016. Fate of

513 Plutonium at a Former Nuclear Testing Site in Australia. Environ. Sci. Technol. 50, 9098–9104.
514 https://doi.org/10.1021/acs.est.6b01864
515 Ikehara, R., Morooka, K., Suetake, M., Komiya, T., Kurihara, E., Takehara, Masato, Takami, R., Kino, C.,
516 Horie, K., Takehara, Mami, Yamasaki, S., Ohnuki, T., Law, G.T.W., Bower, W., Grambow, B.,
517 Ewing, R.C., Utsunomiya, S., 2020. Abundance and distribution of radioactive cesium-rich
518 microparticles released from the Fukushima Daiichi Nuclear Power Plant into the environment.
519 Chemosphere 241, 125019. https://doi.org/10.1016/j.chemosphere.2019.125019
520 Ikehara, R., Suetake, M., Komiya, T., Furuki, G., Ochiai, A., Yamasaki, S., Bower, W.R., Law, G.T.W.,
521 Ohnuki, T., Grambow, B., Ewing, R.C., Utsunomiya, S., 2018. Novel Method of Quantifying
522 Radioactive Cesium-Rich Microparticles (CsMPs) in the Environment from the Fukushima Daiichi
523 Nuclear Power Plant. Environ. Sci. Technol. 52, 6390–6398.
524 https://doi.org/10.1021/acs.est.7b06693
525 Imoto, J., Ochiai, A., Furuki, G., Suetake, M., Ikehara, R., Horie, K., Takehara, M., Yamasaki, S., Nanba,
526 K., Ohnuki, T., Law, G.T.W., Grambow, B., Ewing, R.C., Utsunomiya, S., 2017. Isotopic signature
527 and nano-texture of cesium-rich micro-particles: Release of uranium and fission products from the
528 Fukushima Daiichi Nuclear Power Plant. Sci. Rep. 7, 5409.
529 https://doi.org/10.1038/s41598-017-05910-z
530 Kelley, J.M., Bond, L.A., Beasley, T.M., 1999. Global distribution of Pu isotopes and 237Np. Sci. Total

Environ. 237–238, 483–500. https://doi.org/10.1016/S0048-9697(99)00160-6

Kirchner, G., Bossew, P., De Cort, M., 2012. Radioactivity from Fukushima Dai-ichi in air over Europe; part 2: what can it tell us about the accident? J. Environ. Radioact. 114, 35–40. https://doi.org/10.1016/j.jenvrad.2011.12.016

Konings, R.J.M., Wiss, T., Beneš, O., 2015. Predicting material release during a nuclear reactor accident. Nat. Mater. 14, 247–252. https://doi.org/10.1038/nmat4224

MEXT, GSI, 2012. About the Establishment of the Extension Site of Distribution Map of Radiation Dose, Etc. [WWW Document]. Ext. Site Distrib. Map Radiat. Dose, etc.,/GSI Maps. URL http://ramap.jmc.or.jp/map/ (accessed 12.6.17).

Morrall, P., Price, D.W., Nelson, A.J., Siekhaus, W.J., Nelson, E., Wu, K.J., Stratman, M., McLean, W., 2007. ToF-SIMS characterization of uranium hydride. Philos. Mag. Lett. 87, 541–547. https://doi.org/10.1080/09500830701286227

Nagase, F., Gauntt, R.O., Naito, M., 2016. Overview and outcomes of the OECD/NEA benchmark study of the accident at the Fukushima Daiichi Nuclear Power Station. Nucl. Technol. 196, 499–510. https://doi.org/10.13182/NT16-10

Nishihara, K., Iwamoto, H., Suyama, K., 2012. Estimation of fuel compositions in Fukushima-Daiichi Nuclear Power Plant, JAEA Technical Report. Japan Atomic Energy Agency, JAEA 2012-018, Ibaraki, Japan.

549 Nuclear Emergency Response Headquarters, Government of Japan, 2011. Report of Japanese
550 Government to the IAEA Ministerial Conference on Nuclear Safety - The Accident at TEPCO's
551 Fukushima Nuclear Power Stations - [WWW Document]. URL
552 https://japan.kantei.go.jp/kan/topics/201106/iaea_houkokusho_e.html
553 Ochiai, A., Imoto, J., Suetake, M., Komiya, T., Furuki, G., Ikehara, R., Yamasaki, S., Law, G.T.W.,
554 Ohnuki, T., Grambow, B., Ewing, R.C., Utsunomiya, S., 2018. Uranium Dioxides and Debris
555 Fragments Released to the Environment with Cesium-Rich Microparticles from the Fukushima
556 Daiichi Nuclear Power Plant. Environ. Sci. Technol. https://doi.org/10.1021/acs.est.7b06309
557 Pontillon, Y., Ducros, G., 2010. Behaviour of fission products under severe PWR accident conditions.
558 The VERCORS experimental programme—Part 2: Release and transport of fission gases and
559 volatile fission products. Nucl. Eng. Des. 240, 1853–1866.
560 https://doi.org/10.1016/j.nucengdes.2009.06.024
561 Pontillon, Y., Ducros, G., Malgouyres, P.P., 2010. Behaviour of fission products under severe PWR
562 accident conditions VERCORS experimental programme—Part 1: General description of the
563 programme. Nucl. Eng. Des. 240, 1843–1852. https://doi.org/10.1016/j.nucengdes.2009.06.028
564 Ravel, B., Newville, M., 2005. ATHENA , ARTEMIS , HEPHAESTUS : data analysis for X-ray
565 absorption spectroscopy using IFEFFIT. J. Synchrotron Radiat. 12, 537–541.
566 https://doi.org/10.1107/S0909049505012719

567 Rossberg, A., Reich, T., Bernhard, G., 2003. Complexation of uranium(VI) with protocatechuic acid
568 application of iterative transformation factor analysis to EXAFS spectroscopy. Anal. Bioanal. Chem.
569 376, 631–638. https://doi.org/10.1007/s00216-003-1963-5
570 Sakaguchi, A., Steier, P., Takahashi, Y., Yamamoto, M., 2014. Isotopic compositions of ^{236}U and Pu
571 isotopes in "Black Substances" collected from roadsides in Fukushima prefecture: Fallout from the
572 Fukushima Dai-ichi Nuclear Power Plant Accident. Environ. Sci. Technol. 48, 3691–3697.
573 https://doi.org/10.1021/es405294s
574 Salbu, B., Krekling, T., Lind, O.C., Oughton, D.H., Drakopoulos, M., Simionovici, A., Snigireva, I.,
575 Snigirev, A., Weitkamp, T., Adams, F., Janssens, K., Kashparov, V.A., 2001. High energy X-ray
576 microscopy for characterisation of fuel particles. Nucl. Instruments Methods Phys. Res. Sect. A
577 Accel. Spectrometers, Detect. Assoc. Equip. 467–468, 1249–1252.
578 https://doi.org/10.1016/S0168-9002(01)00641-6
579 Salbu, B., Lind, O.C., 2016. Radioactive particles released to the environment from the Fukushima
580 reactors-Confirmation is still needed. Integr. Environ. Assess. Manag. 12, 687–689.
581 https://doi.org/10.1002/ieam.1834
582 Schwantes, J.M., Orton, C.R., Clark, R.A., 2012. Analysis of a Nuclear Accident: Fission and Activation
583 Product Releases from the Fukushima Daiichi Nuclear Facility as Remote Indicators of Source
584 Identification, Extent of Release, and State of Damaged Spent Nuclear Fuel. Environ. Sci. Technol.

46, 8621–8627. https://doi.org/10.1021/es300556m

Solé, V.A., Papillon, E., Cotte, M., Walter, P., Susini, J., 2007. A multiplatform code for the analysis of energy-dispersive X-ray fluorescence spectra. Spectrochim. Acta Part B At. Spectrosc. 62, 63–68. https://doi.org/10.1016/j.sab.2006.12.002

Steinhauser, G., Brandl, A., Johnson, T.E., 2014. Comparison of the Chernobyl and Fukushima nuclear accidents: A review of the environmental impacts. Sci. Total Environ. 470–471, 800–817. https://doi.org/10.1016/j.scitotenv.2013.10.029

Suetake, M., Nakano, Y., Furuki, G., Ikehara, R., Komiya, T., Kurihara, E., Morooka, K., Yamasaki, S., Ohnuki, T., Horie, K., Takehara, M., Law, G.T.W., Bower, W., Grambow, B., Ewing, R.C., Utsunomiya, S., 2019. Dissolution of radioactive, cesium-rich microparticles released from the Fukushima Daiichi Nuclear Power Plant in simulated lung fluid, pure-water, and seawater. Chemosphere. https://doi.org/10.1016/j.chemosphere.2019.05.248

Taylor, D.M., 1995. Environmental plutonium in humans. Appl. Radiat. Isot. 46, 1245–1252. https://doi.org/10.1016/0969-8043(95)00167-C

Tokyo Electric Power Company Holdings, 2018. Fukushima Daiichi Nuclear Power Station Unit 2 Primary Containment Vessel Internal Investigation Results [WWW Document]. URL http://www.tepco.co.jp/en/nu/fukushima-np/handouts/2018/images/handouts_180201_01-e.pdf

Tokyo Electric Power Company Holdings, 2017. Unit 1 Primary Containment Vessel Internal

603 Investigation [WWW Document]. URL
604 http://www.tepco.co.jp/en/nu/fukushima-np/handouts/2017/images/handouts_170327_01-e.pdf
605 Utsunomiya, S., Furuki, G., Ochiai, A., Yamasaki, S., Nanba, K., Grambow, B., Ewing, R.C., 2019.
606 Caesium fallout in Tokyo on 15th March, 2011 is dominated by highly radioactive, caesium-rich
607 microparticles. ArXiv 1906.00212.
608 Yamamoto, M., Sakaguchi, A., Ochiai, S., Takada, T., Hamataka, K., Murakami, T., Nagao, S., 2014.
609 Isotopic Pu, Am and Cm signatures in environmental samples contaminated by the Fukushima
610 Dai-ichi Nuclear Power Plant accident. J. Environ. Radioact. 132, 31–46.
611 https://doi.org/10.1016/J.JENVRAD.2014.01.013
612 Yamamoto, T., Sakai, T., Iwahashi, D., 2018. Nuclide inventory calculation based on modeled fuel
613 assembly specifications and burnup histories for Fukushima Dai-ichi NPP Units 1–3. J. Nucl. Sci.
614 Technol. 55, 1496–1507. https://doi.org/10.1080/00223131.2018.1527261
615 Yamasaki, S., Imoto, J., Furuki, G., Ochiai, A., Ohnuki, T., Sueki, K., Nanba, K., Ewing, R.C.,
616 Utsunomiya, S., 2016. Radioactive Cs in the estuary sediments near Fukushima Daiichi Nuclear
617 Power Plant. Sci. Total Environ. 551–552, 155–162. https://doi.org/10.1016/j.scitotenv.2016.01.155
618 Zheng, J., Tagami, K., Uchida, S., 2013. Release of Plutonium Isotopes into the Environment from the
619 Fukushima Daiichi Nuclear Power Plant Accident: What Is Known and What Needs to Be Known.
620 Environ. Sci. Technol. 47, 9584–9595. https://doi.org/10.1021/es402212v

621 Zheng, J., Tagami, K., Watanabe, Y., Uchida, S., Aono, T., Ishii, N., Yoshida, S., Kubota, Y., Fuma, S.,
622 Ihara, S., 2012. Isotopic evidence of plutonium release into the environment from the Fukushima
623 DNPP accident. Sci. Rep. 2, 304. https://doi.org/10.1038/srep00304
624
625

626 **Figure caption**

627 Figure 1. Location of Fukushima Daiichi Nuclear Power Plant and sampling location. OTZ and AQC

628 stand for the Ottozawa and aqua culture center in Okuma town, respectively.

629

630 Figure 2. Results of scanning electron microscopy including elemental maps and EDX spectra from

631 three CsMPs; (a) OTZ, (b) AQC1, and (c) AQC2. The images are secondary electron images in (a)

632 and (b), and a back-scattered electron image in (c). The red square in (b) indicates the position of the

633 EDX analysis with a rastered electron beam. The area outlined by the white dotted line indicates the

634 etched hole that resulted from SIMS analysis.

635

636 Figure 3. Results of synchrotron X-ray analysis. (a) Synchrotron micro-focus X-ray fluorescence

637 (μXRF) elemental maps for the entire area of AQC1 outlined by the orange dotted rectangle in Fig.

638 2(b), revealing the distribution of Fe and Zn, collected at beamline X05LA at the Swiss Light

639 Source. The horizontal beam size was ~ 1 μm. High-resolution (step size 0.5 μm) μXRF

640 elemental maps of U, Zr, Mn, and Sr for the area indicated by the white dashed square in the Fe

641 map. (b) Uranium L_3-edge X-ray absorption near-edge structure (XANES) of a discrete point

642 within AQC, indicated by the red arrow in the U $L\alpha$ map. The spectrum is plotted alongside

643 U(IV) and U(VI) oxide standards. (c) Discrete-area Pu L_3-edge XANES collected from the point

644 within AQC indicated by the red arrow in the U *Lα* map. The XANES spectra from the point
645 indicated by the white arrows in the U *Lα* map did not show any Pu absorption edge. The two
646 spectra, one collected from each beamline, displayed after normalization and energy calibration.
647
648 Figure 4. Nano-structure of AQC1 and distribution of discrete U nanoparticles within the CsMP. (a)
649 HAADF-STEM image of FIB thin foil prepared from the area indicated by the red rectangle in Fig.
650 S1a. Yellow arrows and red arrow indicate the position of U nanoparticles labeled U1 – 3 (displayed
651 in Fig. S2) and U4, respectively. STEM-EDX mapping was obtained from the area outlined by the
652 white dotted square and presented accompanied with the HAADF-STEM image. (b) Enlarged
653 HAADF-STEM image of a U nanoparticle (U4) and U elemental map associated with an EDX
654 spectrum obtained with spot analysis on U4. (c) High resolution HAADF-STEM image of U4.
655
656 Figure 5. Uranium and Pu isotopic signature of CsMPs released from units 2 or 3 at FDNPP. (a)
657 $^{235}U/^{238}U$ isotopic ratio of the CsMPs as a function of ion counts (cps/nA) as compared with the
658 values of irradiated and non-irradiated fuels installed in the FDNPP at the time of meltdowns
659 (horizontal lines), which were calculated based on the burnup using the ORIGEN code (Nishihara et
660 al., 2012). For comparison, $^{235}U/^{238}U$ of the volatilized U in the CsMPs (Imoto et al., 2017) is also
661 plotted. (b) The ratios of $^{239}Pu/^{238}U$ and $^{239}PuO/^{238}UO$ ion counts on four spots of analysis for the

three CsMPs. Only the non-oxide form is included for OTZ because of the limited volume of the sample. (c) $^{240}Pu/^{239}Pu$ and $^{242}Pu/^{239}Pu$ isotope ratios of the AQC1 and AQC2 compared with the ratios of bulk soils and litter samples (Zheng et al., 2012), calculated inventory using ORIGEN2 (Nishihara et al., 2012), ORIGEN ARP (Kirchner et al., 2012; Schwantes et al., 2012), and CASMO5 (Yamamoto et al., 2018), the MOX fuels only installed in the FDNPP unit 3 (ORIGEN2 calculation displayed as dashed lines) (Nishihara et al., 2012), and global fallout (Kelley et al., 1999). Error bars exist within the symbols unless otherwise noted.

Table 1. Information on the sampling for CsMPs characterized in the present study. KU-CsMP number and KU-soil number represent a label of CsMP and soil samples in Kyushu University sample archive.

Sample name	KU-CsMP No. KU-soil No.	Latitude−longitude	Distance from FDNPP (km)	Soil type	Sampling date
AQC1	AQC6 KU-161	37°24’27.626”N, 141°01’55.801”E	1.0	surface soil of field	2012/3/16
AQC2	AQC8 KU-171	37°24’27.626”N, 141°01’55.801”E	1.0	surface soil of field	2012/3/16
OTZ	OTZ25 KU-309	37°25’05.570”N, 141°00’21.661”E	3.9	surface soil of field	2017/7/27

Table 2. Size and radioactivity of CsMPs used in this study. The radioactivity of CsMPs was decay-corrected to March 11, 2011.

CsMP	Particle size (μm)	Radioactivity (Bq)		$^{134}Cs/^{137}Cs$ radioactivity ratio	Radioactivity per unit mass (Bq/g)
		^{134}Cs	^{137}Cs		
AQC1	17.8 – 27.9	1176.0 (± 13.0)	1124.2 (± 2.43)	1.05	3.6×10^{11}
AQC2	4.6 – 5.0	13.24 (± 0.18)	11.34 (± 0.04)	1.17	1.6×10^{11}
OTZ	2.6 – 2.8	12.72 (± 0.035)	11.39 (± 0.195)	1.12	1.1×10^{11}

Table 3. Uranium and Pu counts ionized from the CsMPs by SIMS analysis. (a) Ion counts detected as non-oxide. (b) Ion counts detected as oxide. Non-oxide ionized isotopes were measurable at two spots in AQC1, one in AQC2, and one in OTZ. Ions in the oxidized form were successfully determined only for AQC1 and AQC2. Each value is the average of ten scans. The standard deviation is give in the parenthesis. Note that isotope ratio was deduced for each scan leading to better precision than the ion counts. The analytical error in isotope ratio was determined using NIST standard SRM610 and the representative results are given in Supplementary Information Table S1. These isotope ratios are not decay-corrected. Note that these data were subsequently decay-corrected to March 11, 2011 and plotted in Fig. 5

28 (a) Non-oxide ions

Sample	AQC1- spot1	AQC1- spot2	OTZ	AQC2
		Detection non-oxide		
^{235}U (cps)	3.22 (± 0.22)	3.78 (± 0.32)	1.73 (± 0.26)	3.84 (± 1.08)
^{236}U (cps)	0.69 (± 0.14)	0.87 (± 0.05)	0.41 (± 0.13)	0.67 (± 0.35)
^{238}U (cps)	167 (± 11)	195 (± 16)	90 (± 14)	192 (± 48)
^{239}Pu (cps)	0.81 (± 0.1)	0.96 (± 0.08)	0.49 (± 0.15)	1.78 (± 0.68)
Primary beam intensity (nA)	0.2	0.2	0.1	0.2
$^{235}U/^{238}U$	0.01935 (± 0.00009)	0.01935 (± 0.00006)	0.01925 (± 0.00014)	0.01935 (± 0.00011)
$^{236}U/^{238}U$	0.00415 (± 0.00026)	0.00429 (± 0.00008)	0.00447 (± 0.00035)	0.00411 (± 0.00019)
$^{239}Pu/^{238}U$	0.00488 (± 0.00020)	0.00490 (± 0.00010)	0.00534 (± 0.00037)	0.01011 (± 0.00031)

29

30

(b) Oxide ions

Sample	AQC1-spot1	AQC1-spot2	AQC2
Detection oxide			
$^{251}(^{235}UO)$ (cps)	43.89 (± 1.37)	47.89 (± 1.39)	7.77 (±0.73)
$^{254}(^{238}UO)$ (cps)	2268 (± 63)	2470 (± 59)	400 (± 37)
$^{255}(^{239}PuO)$ (cps)	10.89 (± 0.56)	12.05 (± 0.36)	4.18 (± 0.34)
$^{256}(^{240}PuO)$ (cps)	3.800 (± 0.186)	4.145 (± 0.152)	1.140 (± 0.620)
$^{256}(^{241}PuO)$ (cps)	1.290 (± 0.227)	0.935 (± 0.129)	0.380 (± 0.080)
$^{257}(^{242}PuO)$ (cps)	0.730 (± 0.134)	0.785 (± 0.785)	0.260 (± 0.080)
Primary beam intensity (nA)	0.2	0.2	0.2
$^{251}(^{235}UO)/^{254}(^{238}UO)$	0.01935 (± 0.00006)	0.01938 (± 0.00012)	0.01941 (± 0.00006)
$^{255}(^{239}PuO)/^{254}(^{238}UO)$	0.00480 (± 0.00008)	0.00488 (± 0.00005)	0.01047 (± 0.00018)
$^{256}(^{240}PuO)/^{255}(^{239}PuO)$	0.3492 (± 0.0040)	0.3441 (± 0.0033)	0.3313 (± 0.0114)
$^{257}(^{241}PuO)/^{255}(^{239}PuO)$	0.1184 (± 0.0060)	0.0777 (± 0.0036)	0.0904 (± 0.0052)
$^{258}(^{242}PuO)/^{255}(^{239}PuO)$	0.0668 (± 0.0033)	0.0651 (± 0.0011)	0.0622 (± 0.0059)

Figure

Click here to download Figure: Kurihara 2020 STOTEN figures revision1 final.pdf

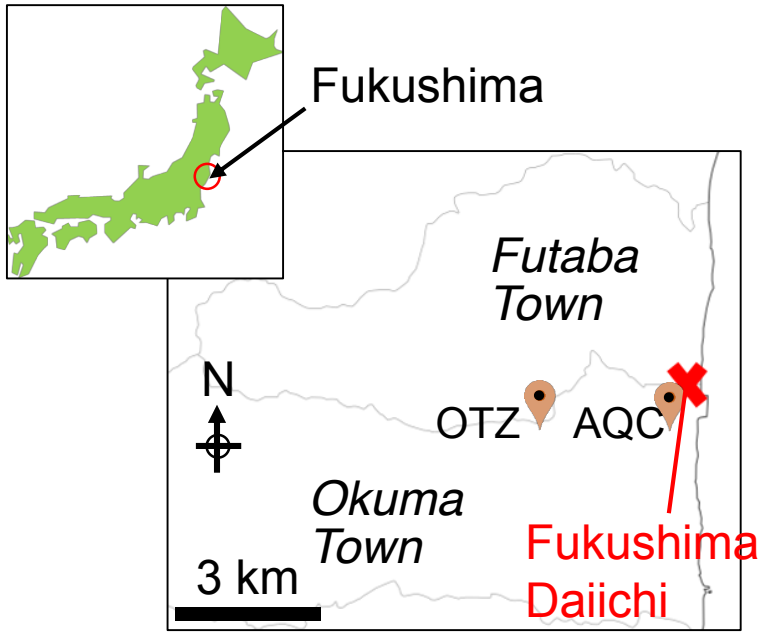

Fig. 1

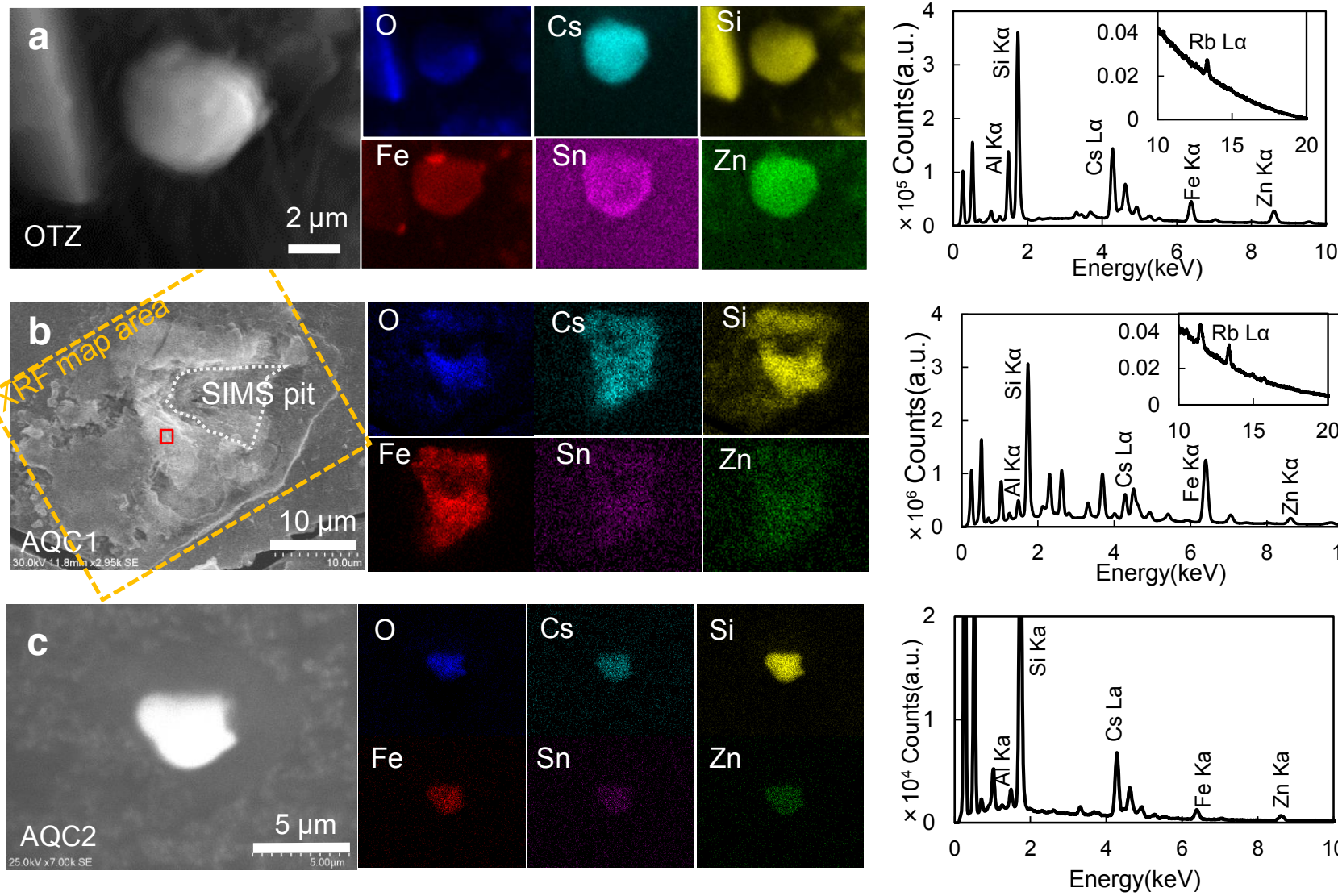
a
OTZ
2 μm
O
Cs
Si
Fe
Sn
Zn
b
XRF map area
SIMS pit
AQC1
10 μm
c
AQC2
5 μm
Si Kα
Al Kα
Cs Lα
Fe Kα
Zn Kα
Rb Lα
Counts(a.u.)
Energy(keV)
Si Ka
Al Ka
Cs La
Fe Ka
Zn Ka

Fig. 2

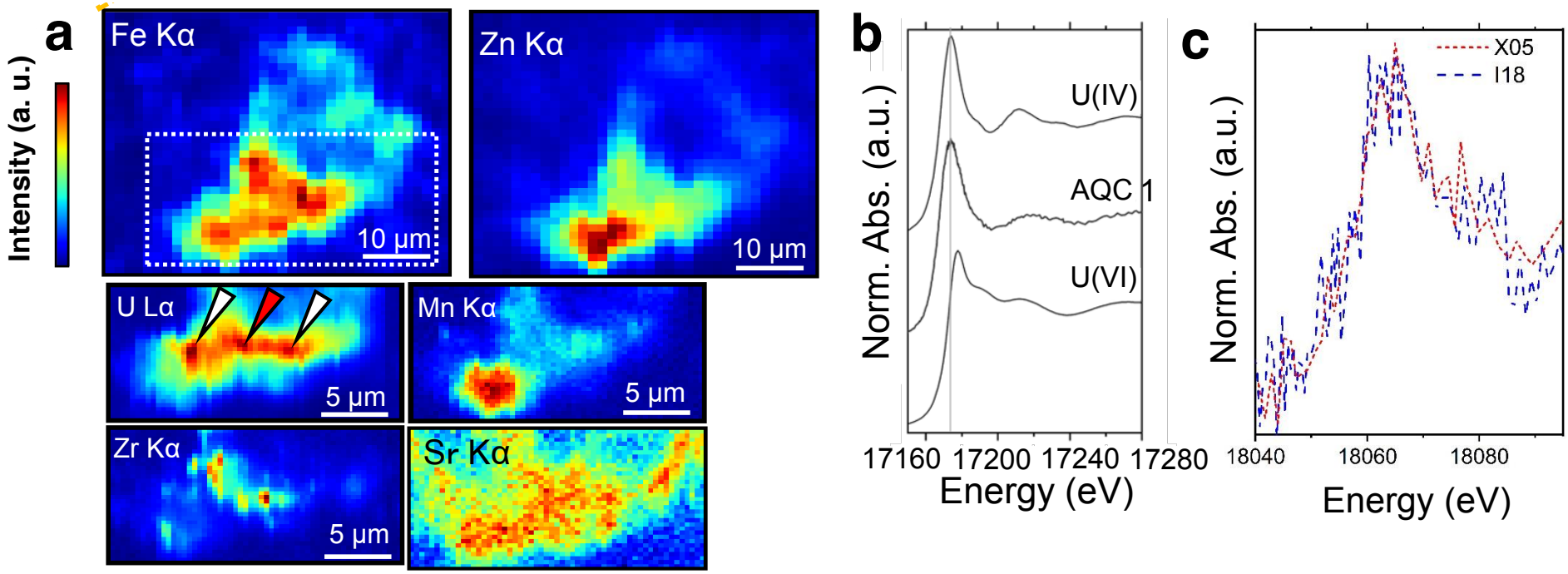
a
Intensity (a. u.)
Fe Kα
10 μm
Zn Kα
10 μm
U Lα
5 μm
Mn Kα
5 μm
Zr Kα
5 μm
Sr Kα
b
Norm. Abs. (a.u.)
U(IV)
AQC 1
U(VI)
17160 17200 17240 17280
Energy (eV)
c
Norm. Abs. (a.u.)
X05
I18
18040 18060 18080
Energy (eV)

Fig. 3

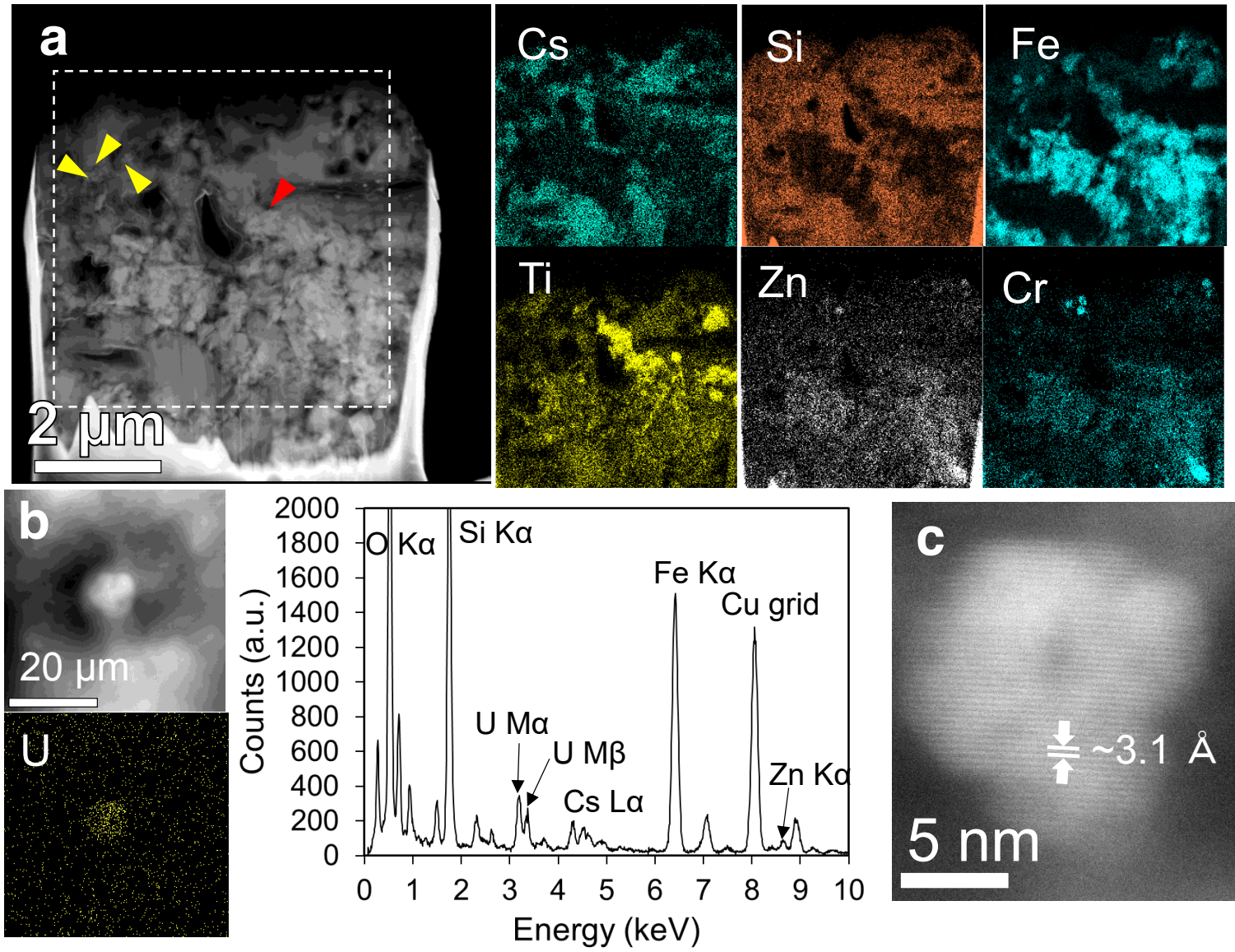
a
2 μm
Cs
Si
Fe
Ti
Zn
Cr
b
20 μm
U
Counts (a.u.)
2000
1800
1600
1400
1200
1000
800
600
400
200
0
O Kα
Si Kα
Fe Kα
Cu grid
U Mα
U Mβ
Cs Lα
Zn Kα
0 1 2 3 4 5 6 7 8 9 10
Energy (keV)
c
~3.1 Å
5 nm

Fig. 4

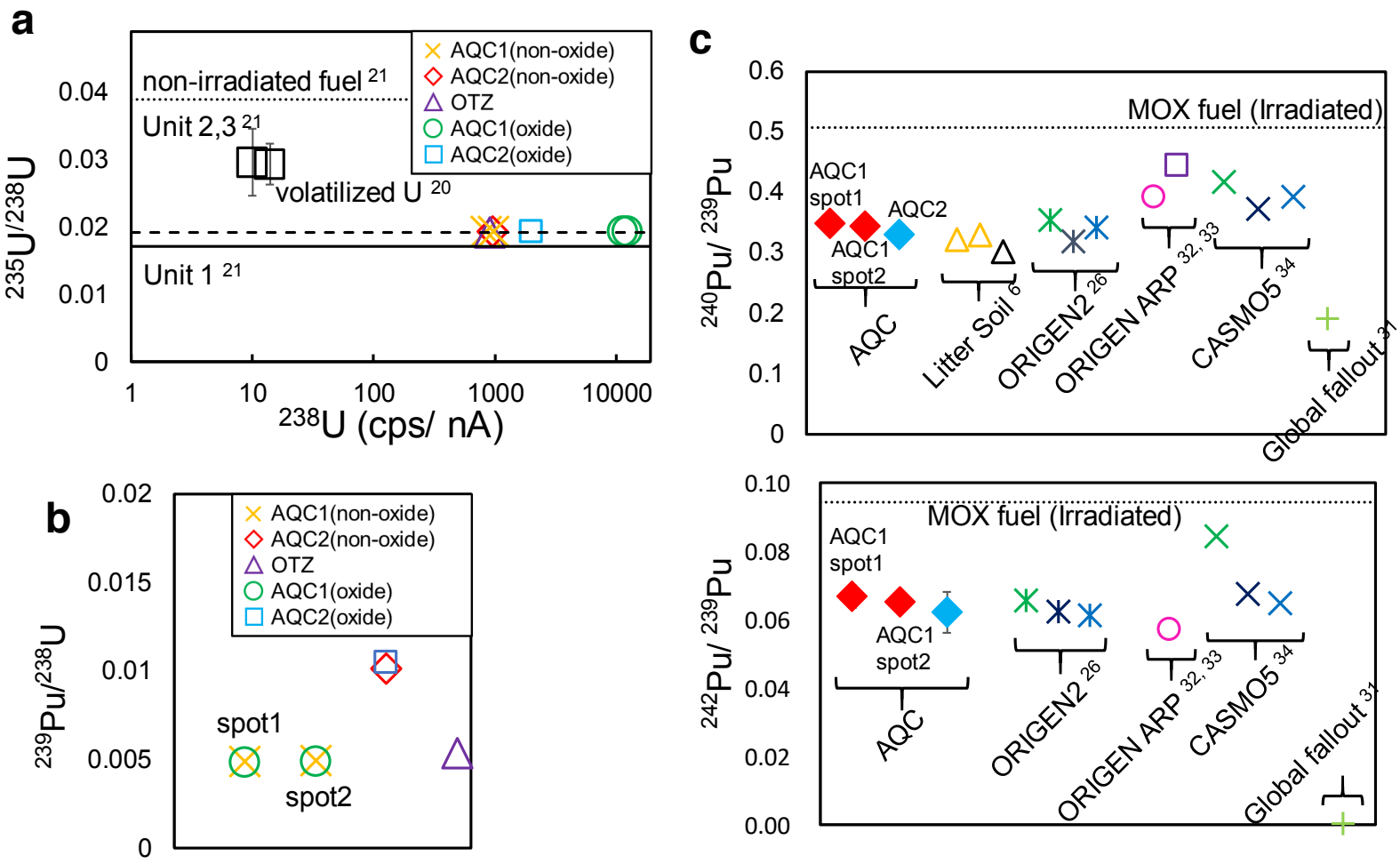

[a] Nishihara et al. (2012), [b] Imoto et al. (2017), [c] Zheng et al. (2012), [d] Kirchner et al. (2012)
[e] Schvantes et al. (2012), [f] Yamamoto et al. (2018), [g] Kelley et al. (1999)

Fig. 5

Supplementary material for on-line publication only

Click here to download Supplementary material for on-line publication only: Kurihara 2020 STOTEN supplementary files revision